

A Nonvolatile Switchable-polarity EPM Valve

Bingchao Wang¹, Jonah Mack¹, Francesco Giorgio-Serchi¹, and Adam A. Stokes^{*1}

¹Soft Systems Group, The School of Engineering, The University of Edinburgh, EH9 3FF Edinburgh, UK

Abstract

Scalable control of pneumatic and fluidic networks remains fundamentally constrained by architectures that require continuous power input, dense external control hardware, and fixed routing topologies. Current valve arrays rely on such continuous actuation and mechanically fixed routing, imposing substantial thermal and architectural overhead. Here, we introduce the Switchable-polarity ElectroPermanent Magnet (S-EPM), a fundamentally new bistable magnetic architecture that deterministically reverses its external magnetic polarity through transient electrical excitation. By reconfiguring internal flux pathways within a composite magnet assembly, the S-EPM establishes two stable, opposing magnetic configurations without requiring sustained power. We integrate this architecture into a compact pinch-valve to robustly control pneumatic and liquid media. This state-encoded magnetic control enables logic-embedded fluidic networks, including decoders, hierarchical distribution modules, and a nonvolatile six-port routing array. These systems provide address-based routing and programmable compositional control, offering features like individual port isolation that are impossible with standard mechanically coupled rotary valves. By embedding functionality in persistent magnetic states rather than continuous power or static plumbing, this work establishes a scalable foundation for digital fluidics and autonomous laboratory platforms. We suggest the reader watches this video demonstration of the valves in action: <https://youtu.be/wEbj6rQ7AOU>

Keywords: S-EPM, S-EPM valve, Magnetic bistability, Zero-power actuation, Fluid transfer, Lab Automation

Advanced applications in automated chemical processing, biomedical diagnostics, and fluid-driven soft robotics require efficient fluid routing and multi-channel switching [1–3]. In chemical automation, dynamic routing enables diverse reaction sequences and parallel sample processing [4, 5], while in soft robotics, multi-channel actuation coordinates motion across multiple degrees of freedom [6–10]. Predominant architectures that rely upon independent pneumatic lines and external solenoid valves are bulky, thermally unstable, and difficult to scale, compromising reagent integrity and limiting robotic maneuverability [11–13]. Consequently, compact and programmable valve systems must efficiently switch multi-channel pneumatic and fluidic media [14–16].

Current fluid routing systems typically rely on mechanically actuated components, such as rotary multiport valves [17, 18]. Although reliable, these devices suffer from inherent limitations—mechanical complexity, large form factors, and high cost—that hinder integration into compact or portable platforms [19]. 3D-printed microfluidic valves offer increased design flexibility and reduced manufacturing cost [20, 21], but they often suffer from poor sealing, limited durability under high pressure, and leakage during switching [21, 22]. Fluidic logic valves eliminate mechanical rotation [23–27], yet these systems require continuous external control signals and lack inherent programmability for autonomous operation [28, 29].

*Corresponding author: adam.stokes@ed.ac.uk

Researchers have explored alternative actuation mechanisms using dielectric or electrorheological (ER) fluids. For instance, soft valves driven by dielectric elastomer actuators (DEAs) use Maxwell stress or electrostatic compression to modulate fluid channels [30, 31]. Similarly, giant electrorheological (GER) fluids or liquid metal electrodes regulate flow [32, 33]. These approaches require hazardous high-voltage inputs (up to 5 kV) and involve complex fabrication processes. Magnetically actuated valves offer a lower-voltage alternative, modulating flow with magnetorheological elastomers (MREs) or fluids (MRFs) [34, 35]. Despite their potential, these magnetic systems suffer from significant thermal drift and continuous power requirements. These flaws compromise the stability of temperature-sensitive fluids. Electropermanent Magnet (EPM)-based valves offer a promising alternative by providing bistable magnetic control without continuous power consumption. Early designs used EPMs to modulate magnetorheological (MR) fluids [36, 37], yet their reliance on magnetic working fluids limits their use in diverse chemical and biological processes. To broaden applicability, EPMs physically block fluid channels by moving ferrous elements [38] or pinching flexible tubing [39, 40]. Such “pinching” mechanisms suit biochemical applications well, as they ensure fluid isolation and prevent contamination from metallic components [17]. Despite these benefits, existing EPM-based valves require complex fabrication. Designers typically optimize them for either pneumatic or liquid media, limiting their versatility. Furthermore, the inherent “on-off” nature of standard EPMs necessitates auxiliary mechanical components for bidirectional movement, hindering system integration and responsiveness[41].

To address these limitations, we introduce the Switchable-Polarity ElectroPermanent Magnet (S-EPM), a fundamentally new magnetic architecture that enables deterministic reversal of external magnetic polarity via transient excitation. Unlike standard EPMs that switch only between magnetized and neutral states, the S-EPM establishes two stable, opposing magnetic configurations by reconfiguring internal flux pathways within a multi-magnet assembly and reversibly magnetizing a low-coercivity Alnico core relative to adjacent high-coercivity NdFeB magnets. This reconfiguration completely and stably reverses the external magnetic field while maintaining bistable, zero-power state retention.

Building upon this S-EPM technology, we developed a programmable valve architecture that routes fluid and switches multiple channels efficiently through five key features: (i) a low-cost, modular architecture using an FDM 3D-printed housing that integrates the S-EPM with an array of permanent magnets; (ii) active bidirectional control enabled by switchable magnetic poles that generate stable attraction and repulsion states to drive a pinching mechanism; (iii) enhanced sample protection through full fluid isolation and excellent thermal performance, where non-contact, pulse-driven operation keeps the system thermally inert and prevents reagent contamination; (iv) high energy efficiency for scale, consuming only 0.6 J per switching event and requiring zero holding power; and (v) broad versatility, supporting pneumatic and hydraulic media while enabling complex combinatorial logic for scalable, autonomous fluidic routing.

1 Results

The Switchable Polarity Electropermanent Magnet (S-EPM)

The Switchable polarity ElectroPermanent Magnet (S-EPM) represents a fundamentally new magnetic architecture that resolves the limitations of standard electropermanent magnets (EPMs) by enabling deterministic external polarity reversal without auxiliary mechanical biasing. The S-EPM comprises a central Alnico magnet (Alnico 500) wound with a copper excitation coil, flanked by two high-coercivity NdFeB magnets (N38SH) (Fig. 1A). Soft-magnetic iron plates enclose the assembly, completing the magnetic flux path and concentrating the external field at the pole interfaces. Detailed fabrication and assembly procedures are provided in SI Appendix, Fig. S2A.

The operating principle of the S-EPM is based on two NdFeB magnets with fixed and opposite axial magnetizations (Fig. 1B and SI Appendix, Fig. S2B). A transient current pulse applied to the surrounding coil reverses the magnetization of the Alnico core. Upon excitation, the reoriented Alnico redistributes the magnetic flux within the assembly. It forms a predominantly internal flux loop with one NdFeB magnet while enhancing the external magnetic flux on the opposite side, as evidenced by the spatial magnetic flux density distributions shown in SI Appendix, Fig. S3. Reversing the pulse inverts the Alnico magnetization and the overall flux configuration, reversing the external magnetic polarity. After pulse removal, the Alnico retains its remanent magnetization. The selected polarity remains stable without continuous power input. The equilibrium between the internal fluid pressure acting on the sealing interface and the magnetic force generated in the magnetized state defines the maximum blocked pressure. We derived the magnetic force following Knaian’s analytical framework[41], with the corresponding geometric parameters and lumped magnetic circuit representation defined in SI Appendix, Fig. S6. This framework models the magnetic circuit through Ampere’s law and the continuity of magnetic flux:

$$\frac{\pi d^2}{12} N_{\text{rods}} \left(B_{\text{Alnico}}(H_m(t), t) + \Delta B_r(t) + 2\mu_0 H_m(t) \right) = \left(\frac{\mu_0 ab}{2g} + \mathcal{P}_{\text{leak}} \right) \left(NI(t) - H_m(t)l \right) \quad (1)$$

where d is the diameter of each permanent magnet, and N_{rods} is the number of magnetic rods in the S-EPM assembly. B_{Alnico} is the magnetic flux density of the Alnico magnet, which is a nonlinear function of the magnetic field $H_m(t)$ and time t due to hysteresis. B_r denotes the remanent flux density of the NdFeB magnets. The term $\Delta B_r(t)$ represents the state-dependent effective remanent contribution arising from the asymmetric flux reinforcement between the Alnico and one of the NdFeB magnets, and can be expressed as $\Delta B_r(t) = 2s_A(t)B_r$, where $s_A(t) \in \{+1, -1\}$ denotes the magnetization state of the Alnico core. μ_0 is the permeability of free space. a and b represent the width and thickness of the magnetic pole pieces, respectively, while g is the effective air-gap length in the magnetic circuit. $\mathcal{P}_{\text{leak}}$ denotes the leakage permeance accounting for flux escaping the principal magnetic path. N is the number of turns in the excitation coil, $I(t)$ is the time-dependent current passing through the coil, and l is the effective magnetic path length of the magnet stack. To predict the magnetic force generated by the S-EPM during its magnetized state, we express the magnetic pressure in the air gap as:

$$p_m = \frac{B_g^2}{2\mu_0}, \quad F = \mu_0 ab \left(\frac{NI(t) - H_m(t)l}{2g} \right)^2 \quad (2)$$

where p_m denotes the magnetic pressure corresponding to the energy density stored in the air gap. F represents the magnetic force generated by the S-EPM during its magnetized state. The magnetic energy density method calculates F by applying the magnetic pressure over the effective pole area (ab) to yield the total attractive force across the gap. B_g is the magnetic flux density within the air gap derived from the magnetic-circuit relation. As shown in Equation (2), the magnetic force depends on the geometric dimensions of the S-EPM. The air gap g plays a dominant role in determining the force magnitude. A more detailed theoretical formulation and derivation of the analytical framework are provided in SI Appendix, Section S6. We wound the S-EPM coils with 150 turns of 35 AWG wire to balance energy efficiency with the required magnetic force. This wire gauge and coil geometry lower the electrical resistance, ensuring the necessary transient current is available for fast, reliable switching. We apply a 48 V pulse lasting 1 ms to drive the coil (SI Appendix, Fig. S5). This elevated power rapidly and uniformly reorients the magnetic domains, minimizing the hysteresis delay between the applied field and the resulting magnetization. The optimized design and validated drive method consume approximately 0.6 J per switching cycle.

S-EPM valve design

The S-EPM valve integrates a bistable magnetic actuator within a compact pinch-valve architecture to switch deterministically between two fluidic channels (Fig. 2A and Movie S1). The assembly comprises four primary components: (i) the S-EPM actuator, (ii) a rigid PLA housing fabricated via FDM 3D printing, (iii) two parallel silicone tubes (outer diameter 2 mm, inner diameter 1.5 mm), and (iv) sixteen static N40 permanent magnets (5 mm diameter, 7 mm length) arranged in four vertically aligned groups around the actuator. Magnets positioned along opposing vertical axes present opposite poles toward the S-EPM, establishing a vertical magnetic force gradient when the actuator polarity reverses. The housing incorporates two raised internal bars on both the upper and lower inner surfaces, aligned with the S-EPM end caps. These protruding features concentrate the contact area between the S-EPM and the silicone tubing. This design increases the local compressive stress and ensures reliable tube occlusion under the available magnetic force.

A transient voltage pulse (1 ms) applied to the coil surrounding the Alnico core reverses its magnetization. This pulse redistributes the magnetic flux within the assembly (Fig. 2B). Polarity switching modifies the magnetic interactions between the S-EPM and the surrounding fixed magnet arrays, displacing the actuator vertically through alternating attraction and repulsion.

In the configuration that Fig. 2C(i) shows, the lower tube is compressed (closed) while the upper tube remains open. As Fig. 2C(ii) illustrates, the lower magnet array attracts the S-EPM and the upper array repels it, producing a net downward magnetic force. This force drives the actuator downward, compressing the lower silicone tube and blocking flow. Simultaneously, it releases the upper channel. A negative excitation pulse (pulse polarity = -1) establishes this magnetic configuration, as Fig. 2C(iii) shows. The pulse reverses the magnetization of the Alnico core and creates a clockwise flux loop within the Alnico.

Reversing the excitation pulse produces the complementary configuration that Fig. 2D shows. In Fig. 2D(i), the upper tube is compressed while the lower tube remains open. As Fig. 2D(ii) depicts, the system attracts the S-EPM upward and repels it downward, generating a net upward force that displaces the actuator and seals the upper channel. A positive excitation pulse (pulse polarity = $+1$) achieves this state. The pulse reverses the Alnico magnetization and establishes a counterclockwise flux loop within the Alnico (Fig. 2D(iii)), inverting the magnetic interaction pattern.

Because of the remanent magnetization of the Alnico core, each actuation state remains mechanically stable after removal of the excitation pulse, enabling bistable operation without continuous power input. We evaluate valve performance by measuring the maximum blocked pressure, defined as the critical internal pressure the valve can withstand without leakage.

Characterization of the S-EPM valve’s pressure blocking capability

To integrate the S-EPM valve effectively into configurable fluidic systems, we characterized the device across five performance metrics: dynamic blocking capacity, cyclic switching reliability, switching dynamics, temporal sealing stability, and static pressure limits. We adapted the experimental apparatus for evaluating blocking performance from Moran’s methodology [39] (Fig. 3A). We directed compressed air from a regulated supply through a flow meter and an upstream pressure sensor (P_{in}) to the valve inlet. We connected the valve outlet to a downstream pressure sensor (P_{out}) and a high-resistance venting element, allowing controlled depressurization to the atmosphere (Fig. 3B). This configuration enabled precise quantification of the differential pressure maintained across the valve in the blocked state.

We characterized the switching performance of the S-EPM valve by analyzing pressure transients as the system toggled the measured channel between open and closed states. We aimed to verify the capacity of the valve to isolate the inlet from the outlet. This isolation maintains pneumatic energy in downstream actuators and prevents unintended dissipation. Upon

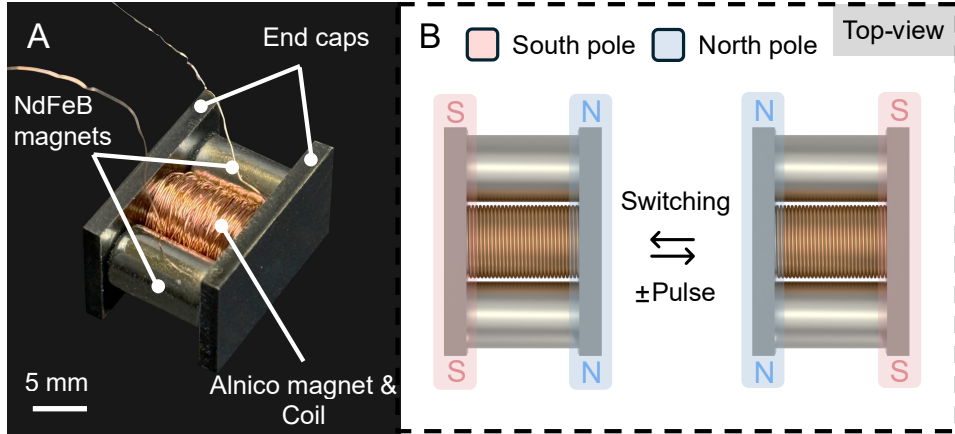


Figure 1: **Switchable ElectroPermanent Magnet (S-EPM) architecture and polarity switching mechanism.** (A) S-EPM assembly components. (B) Labelled magnetic poles of the Switchable Electrostatic Permanent Magnet (S-EPM) in both switched states.

actuation, the valve exhibited distinct flow behaviors. During the closed-to-open transition, the downstream region rapidly equilibrated with the supply pressure, ensuring effective flow transmission. Conversely, the open-to-closed transition triggered a near-instantaneous venting of the outlet to ambient levels while the inlet pressure remained stable. These switching dynamics allow the valve to block flow selectively and sustain high differential pressures.

To assess performance under significant differential loads, we evaluated the dynamic blocking capability of the valve at supply pressures ranging from 310 to 320 kPa. As the pressure-time curves show (Fig. 3C(i)), the outlet pressure dropped abruptly to ambient levels upon actuation across all tested pressures. The inlet side reliably sustained the supply load. To verify consistent blocking performance across a broader operational spectrum, we conducted additional tests at 50, 125, and 200 kPa (SI Appendix, Fig. S7). This consistent, leakage-free response at pressures up to 320 kPa demonstrates the valve’s robust sealing integrity for high-pressure applications. We assessed operational reliability through cyclic switching tests at a nominal pressure of ≈ 50 kPa (Fig. 3C(ii)). These experiments yielded highly reproducible pressure profiles. The downstream region promptly equilibrated with the inlet during opening and vented rapidly during closing. We observed no signal drift or amplitude degradation over repeated cycles, confirming consistent flow-blocking and transmission performance under frequent actuation.

High-resolution analysis at an inlet pressure of approximately 100 kPa quantified the dynamic response speed. The transition from the open to the closed state depressurized the outlet within 0.115 s (Fig. 3D(i)). This rapid closure induced a momentary pressure spike at the inlet due to the sudden arrest of flow. The spike quickly dissipated as the system returned to steady state, validating the swift closure mechanism without compromising upstream stability. To characterize the switching latency between alternate flow paths, we employed a dual-outlet experimental setup (Fig. 3D(ii)). The recorded pressure profiles displayed a synchronized alternating pattern; the pressurization of one outlet channel coincided with the venting of the other. The crossover transition occurred within a < 0.5 s window. This verifies the intrinsic bistable operation of the S-EPM, where only one fluidic path remains active at any given time.

Long-duration and high-pressure static tests further investigated leakage behavior in the closed state. As Fig. 3E(i) shows, we subjected the valve to a constant supply pressure of ≈ 300 kPa for 20 minutes. The outlet pressure remained at ambient levels with negligible fluctuations. This demonstrates that leakage does not accumulate over time and the blocking function remains stable throughout extended operation. Furthermore, as Fig. 3E(ii) illustrates, we incrementally increased the upstream pressure from 300 to 500 kPa. Despite this substantial increase in differential pressure, the outlet trace showed no discernible rise. The sealing integrity

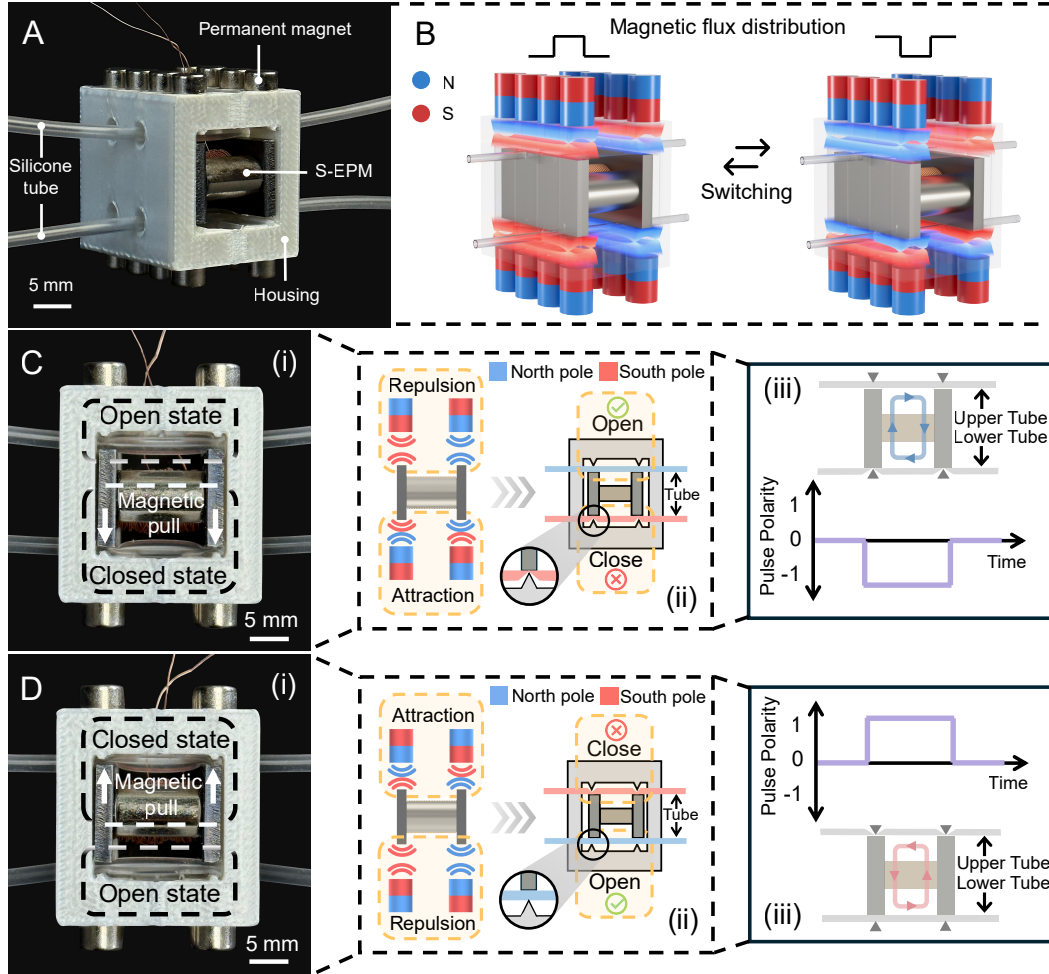


Figure 2: **Design and operating principle of the S-EPM valve.** (A) Photograph of the assembled valve, showing the silicone tubing, 3D-printed housing, central S-EPM actuator, and sixteen permanent magnets arranged in four vertically aligned arrays (four magnets per group). (B) Magnetic flux distribution under opposite magnetization states of the S-EPM, illustrating polarity switching within the assembly. (C) Downward actuation state. (i) Photograph of the valve with the lower tube compressed (closed) and the upper tube open. (ii) Schematic of the magnetic configuration with a magnified view of the lower tube deformation, highlighting compression-induced occlusion. (iii) Corresponding excitation pulse (pulse polarity = -1) and clockwise magnetization of the Alnico core. (D) Upward actuation state. (i) Photograph of the complementary configuration with the upper tube closed and the lower tube open. (ii) Schematic of the alternate magnetic configuration with a magnified view of the uncompressed lower tube. (iii) Corresponding excitation pulse (pulse polarity = $+1$) and counterclockwise magnetization of the Alnico core.

of the valve remains insensitive to inlet pressure variations within this regime. These results confirm that the valve maintains a leakage-free state without performance deterioration, even when pushed to the 500 kPa upper limit of the testing apparatus.

Despite these successful static tests, we identified a performance threshold at the dynamic blocking pressure of ≈ 320 kPa, revealing a constraint in the instantaneous force generation. At this level, a single current pulse successfully reversed the magnetic polarity. Yet, the resulting electromagnetic force occasionally failed to compress the tubing fully against the high internal pressure in a single stroke. The failure to fully compress the tube necessitated successive activation pulses to establish a stable seal. The infrequent failure to fully occlude the channel suggests that

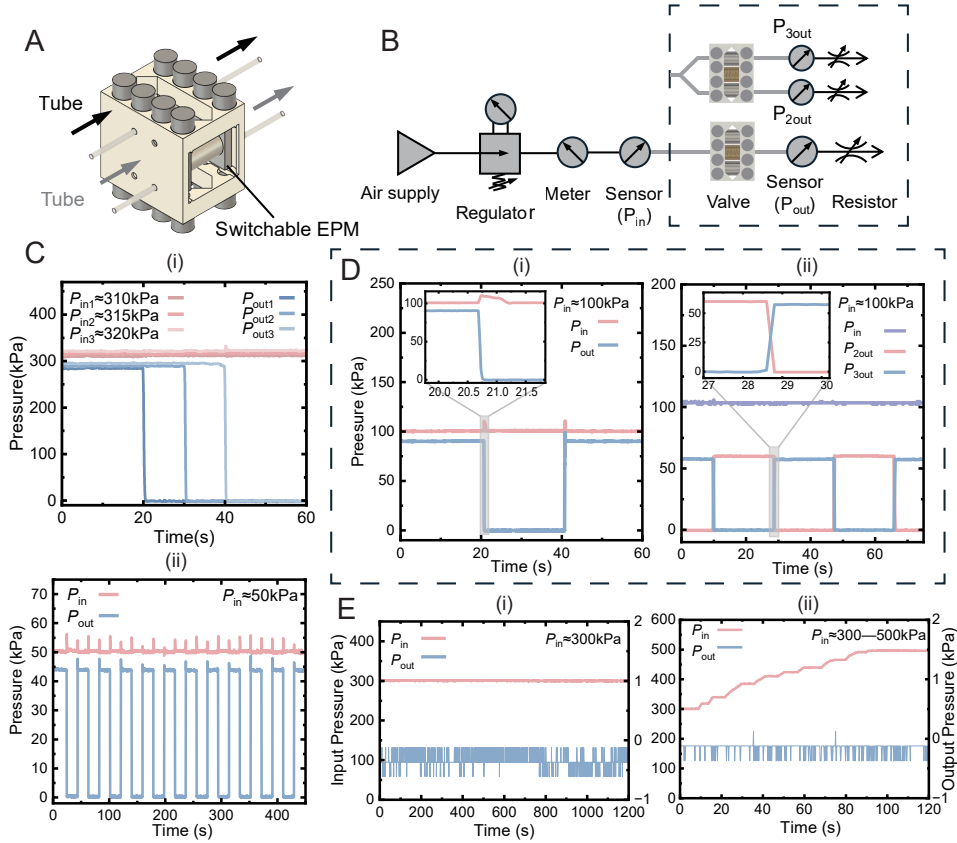


Figure 3: **Pressure blocking characterization of the S-EPM valve.** (A) Photograph of the S-EPM valve integrated with compressible tubing. (B) Experimental setup for pressure-blocking measurements, including regulated air supply, flow meter, upstream (P_{in}) and downstream (P_{out}) pressure sensors, and venting resistor. (C) Dynamic blocking performance: (i) pressure–time traces at $P_{in} \approx 310, 315,$ and 320 kPa; (ii) cyclic switching at $P_{in} \approx 50$ kPa. (D) Transient switching dynamics at $P_{in} \approx 100$ kPa: (i) time-resolved single-channel switching transient; (ii) dual-outlet alternating operation showing complementary pressurization profiles. (E) Static sealing tests (Note: Double Y-Axis shows detailed results for P_{out} , noise due to analog-to-digital conversion) (i) long-duration blocking at $P_{in} \approx 300$ kPa for 20 min with stable upstream pressure and ambient outlet levels; (ii) stepwise upstream pressure ramp from 300 to 500 kPa with corresponding P_{in} and P_{out} traces.

while the valve maintains high pressure-bearing potential, optimizing the actuation protocol or refining the S-EPM core positioning could further enhance reliable dynamic operation at such extremes.

Multi-Modal Fluidic Control Architectures enabled by S-EPM Valves

Laboratory automation requires programmable fluid handling. Experimental workflows routinely selectively deliver, mix, and route liquids among multiple reservoirs, reaction sites, and output channels [2, 42]. Current approaches rely on numerous individual valves and extensive external pumping infrastructures. These resulting complex control architectures face significant scalability challenges as system size grows [43].

At the system level, we can abstract many laboratory operations as address-based fluid selection and routing tasks, analogous to the operation of decoders and multiplexers in digital logic. Translating this abstraction into the fluidic domain remains challenging. Standard valve-based control architectures introduce substantial integration, actuation, and energy overhead as

the number of controlled elements increases [2, 44].

To address these limitations, we realized decoder- and multiplexer-like logic within fluidic networks of S-EPMs. This integrated S-EPM combination enables address-based routing and distribution without continuous actuation. It leverages the inherent bistability of S-EPM technology. We integrated S-EPM valves into diverse architectural configurations to achieve low-

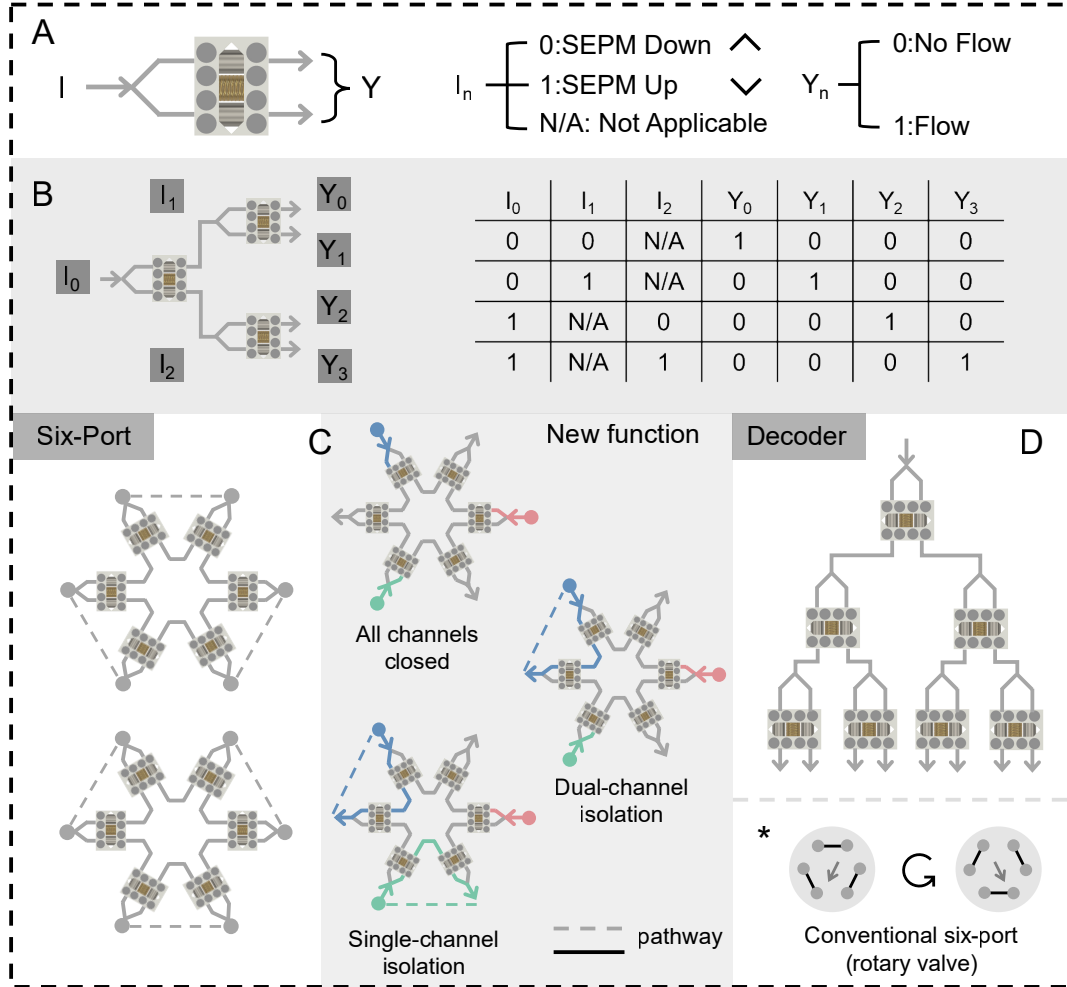


Figure 4: **Architectural configurations of S-EPM-based fluidic routing.** (A) Binary routing unit. A single S-EPM valve encodes two bistable magnetic states corresponding to flow (1) or no flow (0). (B) Hierarchical tree-like routing module. A single input (I_0) is distributed to four outputs (Y_0 – Y_3) through three cascaded valves. The associated truth table defines the deterministic mapping between valve states and the activated output port, where 0 and 1 denote the two stable logical states of an S-EPM valve (no flow and flow, respectively), and N/A indicates a state irrelevant to the selected routing outcome. (C) Six-port configuration arranged in an alternating input-output sequence around a circular topology. State-encoded control enables routing between adjacent ports and supports independently programmable modes including “All channels closed,” “Single-channel isolation,” and “Dual-channel isolation.” For comparison, a conventional mechanically actuated six-port rotary valve is shown, illustrating its fixed routing pathways and limited reconfigurability. (D) Decoder-like routing configuration in which collective valve states encode a binary address to select a specific output channel from a single input.

power, combinatorial fluidic routing (Fig. 4 and SI Appendix, Fig. S4), including representative dual-valve and triple-valve implementations (Movie S2). At the fundamental level (Fig. 4A), a

single bistable S-EPM valve encodes a binary routing state, enabling or blocking flow without static power consumption. Leveraging this principle, we implemented a hierarchical tree-like topology (Fig. 4B). In the four-output configuration shown, three cascaded valves collectively determine the routing path of a single fluidic input (I_0). They direct it to one of four outputs (Y_0 – Y_3) through successive branching decisions. The associated truth table explicitly defines the mapping between valve states and the activated output port, establishing a deterministic correspondence between magnetic state programming and fluidic address selection.

A Nonvolatile Dual-Tree distribution via cooperative S-EPM valve modules

Modular S-EPM valve groups coordinate to achieve Dual-Tree distribution (Fig. 5C). The physical implementation features two identical valve modules positioned symmetrically around a central mixing unit (Fig. 5B). Each module comprises three S-EPM valves with a single input and four controllable output branches. While these two modules are independently addressable, they fluidically couple to the same downstream mixing module.

To enable versatile liquid handling, the FDM 3D-printed central mixing module uses a stacked configuration of internal flow channels (Fig. 5A). This architecture allows the system to combine reagents from the upstream valves or route them separately before they exit through the bottom. By positioning a six-well plate beneath the module and reprogramming the S-EPM valve states, the system dynamically determines the distribution pattern. This architecture provides a choice between pristine reagent delivery or on-chip mixing. The functional versatility of this distribution logic is demonstrated using red and blue dyes as representative inputs (Fig. 5C). Combining the dyes produces a purple output, visually confirming successful mixing. The system facilitates programmable one-to-many distribution. In one specific configuration, certain wells receive mixed reagents while others receive individual dyes. Upon transitioning to an alternate state, the system reconfigures these roles. This outcome demonstrates that the physical architecture supports multiple, distinct distribution topologies.

A representative valve state sequence demonstrates the logic-driven nature of these transitions (Fig. 5D and Movie S3). The values +1 and -1 denote the two stable states of each S-EPM valve. We organize the sequence into two rows (Valves 1–3 and 4–6), with each column representing a discrete system configuration. The well-plate schematics at the base of each column confirm the resulting reagent distribution for that state. This representation proves that system transitions are logic-driven rather than time-dependent, highlighting the inherent architectural flexibility of the S-EPM-based design.

Six-port routing via modular S-EPM valve arrays While the cooperative modules excel at one-to-many distribution, we also reconfigured the modular S-EPM architecture into a circular array to replicate and enhance current routing paradigms. The six-port rotary valve is a staple of fluid routing in chemistry and life-science laboratories. It enables deterministic switching between predefined flow paths. Although widely employed in automated systems, such as the platform demonstrated by Steiner [45], current rotary valves rely on bulky electromechanical actuation and suffer from mechanically coupled flow paths, moving parts, high cost, and limited repairability.

Implementing a six-port routing architecture via a circular array of modular S-EPM valves (Fig. 4C) replicates this familiar routing paradigm while providing expanded operational flexibility. Arranging these valves in a ring to form a reconfigurable junction extends the capabilities of current rotary valves—which rely on bulky electromechanical actuation—without altering the physical layout. As shown in the physical realization (Fig. 6C), a single pump pneumatically drives three independent reagents into the module through alternating input valves (Valves 1, 3, and 5). Two neighboring output valves (Valves 2, 4, and 6) flank each input. Reprogramming the input valve state directs the reagent toward either neighbor.

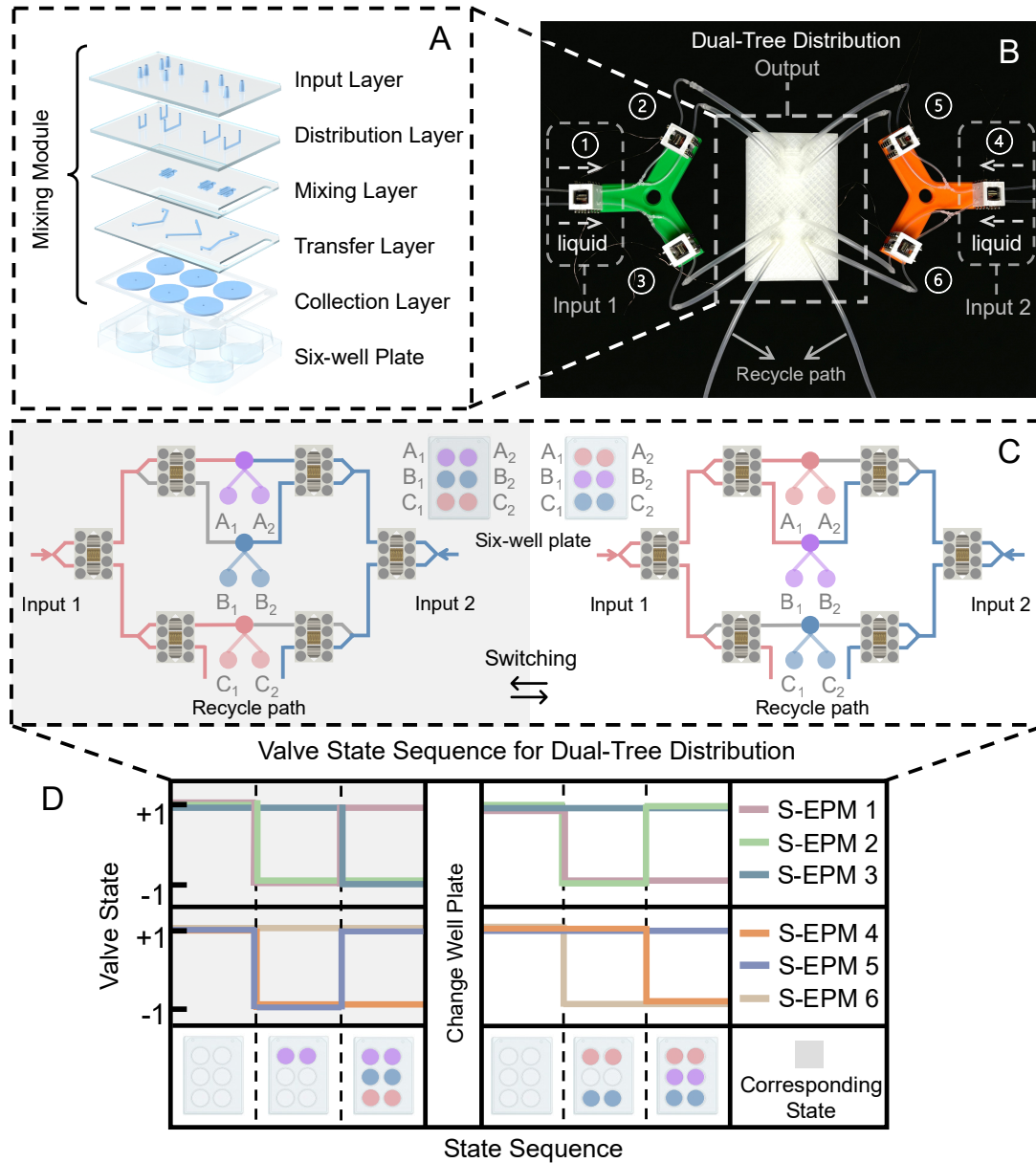


Figure 5: **Nonvolatile dual-tree distribution and mixing via cooperative S-EPM valve modules.** (A) Layered architecture of the FDM-fabricated mixing module, comprising input, distribution, mixing, transfer, and collection layers for vertically integrated flow management, with outputs directed into a six-well plate. (B) Physical implementation of the dual-tree mixer, featuring two symmetric three-valve S-EPM modules coupled to a central mixing unit with a shared downstream output. (C) Reconfigurable mixing behavior in the dual-tree architecture demonstrated using red and blue dyes as representative inputs. Upon interaction, the two streams produce a purple output, enabling direct visualization of mixing. By switching the valve states, the system transitions between two configurations, resulting in a shift of the mixing region across the six-well plate. The labeled nodes (A1–C2) correspond directly to individual wells, highlighting programmable control over both routing and the spatial location of mixing, with excess flow directed through defined recycle paths. (D) Representative valve state sequence governing dual-tree operation. Values +1 and -1 denote the two stable states of each S-EPM valve. Each column corresponds to a distinct system configuration, with the well-plate schematics indicating the resulting distribution pattern. The grey panels in (D) correspond to the grey-highlighted distribution states shown in (C).

Crucially, the independent addressability of each output valve enables an “Individual Routing Mode.” This isolates a single output, a functionality fundamentally inaccessible to current coupled six-port valves that rely on bulky electromechanical actuation and mechanically linked flow paths. We extend this logic to the Selective Addressing of the array. This enables configurations such as All closed, Two closed, or Single closed to isolate any combination of output ports according to workflow requirements.

A representative routing demonstration (Fig. 6A and Movie S4) showcases the versatility of this architecture. In the first state, the system establishes three parallel paths (e.g., Valve 1 to 2, 3 to 4, 5 to 6), delivering pristine reagents to the well plate. Upon a global switching event, the system transitions to a second state where the input valves select the alternate adjacent paths (e.g., Valve 1 to 6, 3 to 2, 5 to 4). This reconfiguration allows each well to receive a combination of two reagents. It demonstrates a transition from parallel to combinatorial routing without any change to the physical hardware. This transition highlights the capacity of the S-EPM array to dynamically redefine its routing topology through software-defined state changes.

Decoder operation based on modular S-EPM valves

We constructed a fluidic decoder by arranging S-EPM valves into a tree-like network. This network selectively routes a single input to one of multiple output branches through discrete valve state combinations (Fig. 4D and Movie S5). In this configuration, seven S-EPM valves address eight independent output paths, decoding a single control input into spatially distributed fluidic outputs. Interpreted inversely, the same architecture functions as a multiplexer. It selects one branch among multiple candidates to connect to a shared channel, depending on the programmed valve states. To integrate distribution and compositional control within this network, we developed the eight-valve mix-decoder module (Fig. 6D). This physical realization uses a single external pump to supply various fluid media under continuous driving pressure. The system governs the selection and routing of each medium solely through encoded S-EPM valve states. This enables seamless transitions between simple distribution and complex, compositionally controlled routing without modifying the physical layout. In the experimental setup (Fig. 6B), tubing connects each color-coded output port to a designated well in the cell plate. This provides a direct visual mapping between routing states and spatially addressed wells.

The valve state sequence (Fig. 6E and Movie S5) demonstrates the dynamic execution of this mix-decoder logic. In this example, we supply two distinct fluid media to the input. S-EPM 1 switches between logical states +1 and -1 to select the delivered medium at each step. This programmed sequence alternates between liquid and gas over multiple 1.5 s intervals, followed by a final 2 s gas phase. Together, they form a complete 9.5 s control cycle.

After each cycle, the system sequentially advances the decoder valve states to redirect the input stream to a subsequent output branch. Each 9.5 s cycle targets a single well of the cell plate. Repeating this process addresses all eight wells using identical control logic and timing. This operation demonstrates how integrating temporal encoding at the input with spatial decoding enables the programmable distribution of mixed media. Throughout this work, +1 and -1 denote the two stable logical states of an S-EPM valve, independent of the driving pulse polarity.

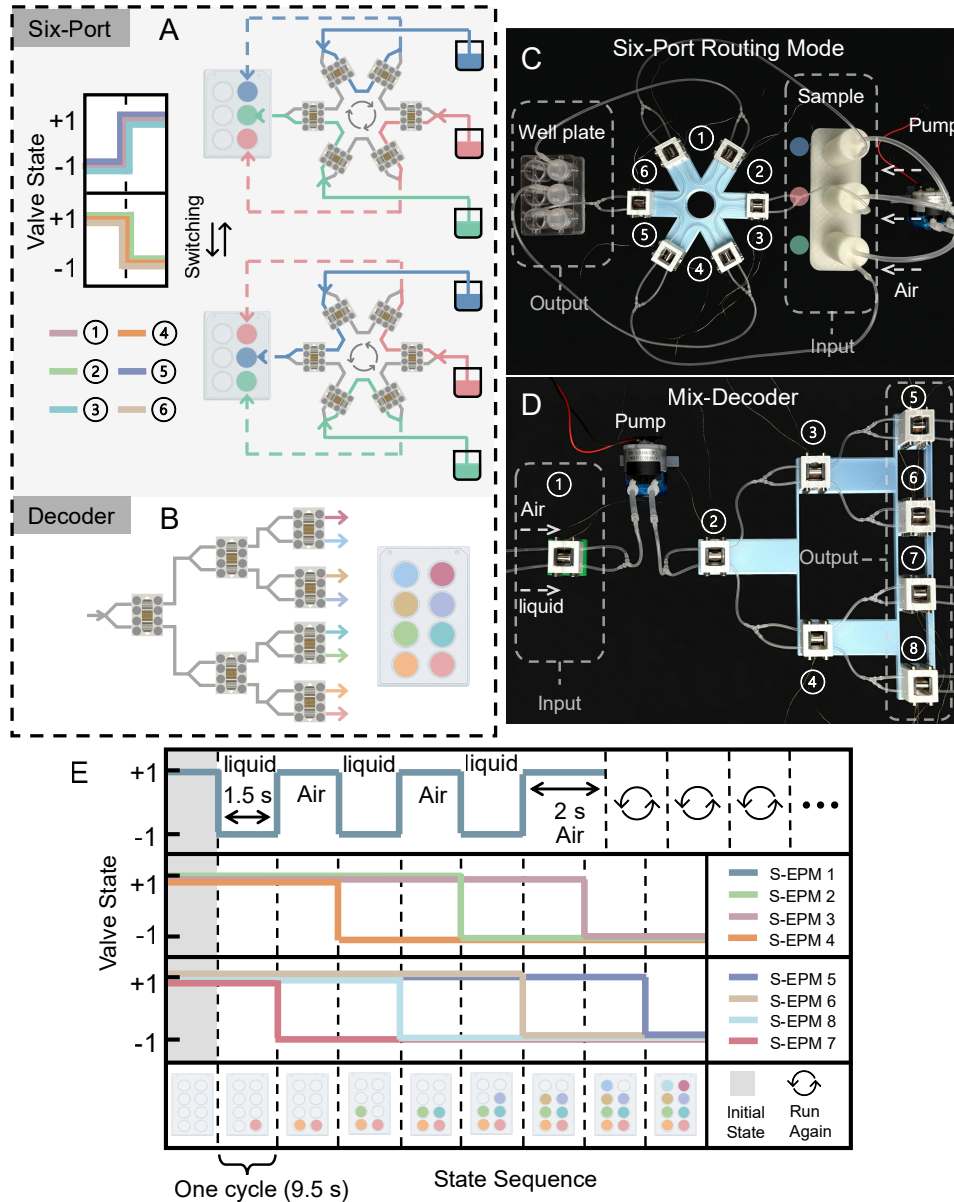


Figure 6: **Reconfigurable routing and decoding demonstrations using modular S-EPM valve architectures.** (A) Six-port routing demonstration showing a transition from three parallel delivery paths (pristine reagents) to an alternate configuration in which each input is redirected to the adjacent branch. The corresponding S-EPM valve state sequences (+1 / -1) are shown above each routing configuration. (B) Experimental visualization of the mix-decoder setup, where color-coded output ports are connected via tubing to designated wells in a cell plate. (C) Physical realization of the six-port S-EPM valve array arranged in a circular topology and driven by a single external pump, with alternating ports forming a reconfigurable routing junction. (D) Eight-valve mix-decoder module that integrates distribution and compositional control within a single network under continuous driving pressure. (E) Time-sequenced valve state control for mix-decoder operation. Values +1 and -1 denote the two stable states of each S-EPM valve. Each column represents a discrete configuration within a 9.5 s control cycle, with the corresponding well-plate schematics indicating the resulting distribution pattern. Upon completion of one cycle, the decoder states advance to address the next output branch, enabling sequential well addressing under identical timing logic.

These demonstrations establish a unified framework for logic-inspired fluidic control. Dis-

crete valve states, rather than fixed plumbing, govern routing, distribution, and compositional operations. By decoupling fluidic functionality from physical topology, we reconfigure complex workflows on demand through software-defined programming. Importantly, this architecture replicates and extends classical components such as the six-port rotary valve by introducing independent path selection and persistent operation without sustained power input. Consequently, S-EPM-based systems offer a scalable, energy-efficient, and highly reconfigurable route toward the next generation of programmable laboratory automation.

System-level integration in extravehicular scenarios

To demonstrate system-level capabilities in human-interfacing scenarios, we implemented a wearable assistive platform based on stacked S-EPM valves, specifically designed for the rigors of extravehicular activities (EVA). This system facilitates dual-functional integration: pneumatic assistance to enhance finger dexterity within pressurized astronaut gloves (SI Appendix, Fig. S1A-C and Movie S6) and programmable thermal regulation via multi-channel fluidic routing in cooling garments (SI Appendix, Fig. S1D and Movie S7). By overcoming the intrinsic stiffness of pressurized gear and enabling precise localized temperature control, these demonstrations underscore the versatility of the S-EPM architecture as a robust foundation for next-generation integrated wearable fluidic systems (SI Appendix, Section S1).

2 Discussion

The development of the Switchable-polarity ElectroPermanent Magnet (S-EPM) resolves a long-standing limitation of standard EPMS: the inability to dynamically reverse polarity without auxiliary mechanical biasing[41]. By modulating internal flux paths to achieve bistable push-pull states, we created a valve architecture that combines the energy efficiency and thermal stability of permanent magnets with the controllability of active solenoids. Because we encode each valve state magnetically and maintain it without continuous power input, actuation no longer requires persistent external control signals or antagonistic mechanical biasing. This innovation mitigates a structural limitation of current fluidic control architectures, where functional complexity scales linearly with the number of externally driven valves and control channels[43, 46].

The S-EPM valve features multi-modal versatility. Soft microfluidic valves are limited to low pressures and specific media[26, 47]. Commercial solenoid valves suffer from substantial Joule heating [48]. Our system bridges the gap between pneumatic power and biological compatibility. The valve blocks pressures up to 500 kPa statically and 320 kPa dynamically. This performance far exceeds the range of typical dielectric or hydrogel-based actuators[30, 49, 50], making the valve suitable for driving high-force soft robotic effectors. Simultaneously, the zero-power holding state ensures the system remains thermally inert. This thermal stability prevents reagent degradation and enzymatic reaction rate shifts during biochemical workflows[51, 52].

Beyond individual component performance, the S-EPM framework shifts laboratory automation toward “digital fluidics” through architectural scalability. The fluidic decoders and multiplexers illustrate how S-EPM modules execute combinatorial logic. This logical mapping decouples the number of controlled outputs from the number of active drive signals. This capability mirrors the transistor-to-logic-gate transition in electronics. It offers a pathway to autonomous, self-contained fluidic computers that do not rely on massive banks of external valves.

Furthermore, our nonvolatile replication of the six-port rotary valve challenges a ubiquitous standard in analytical chemistry. Mechanical rotary valves handle pressure exceptionally well, but they are mechanically rigid, expensive, and limited to fixed routing topologies. The S-EPM array matches and extends the functional logic of these components. It introduces an “Individual Routing Mode” impossible with coupled mechanical rotors. This independence allows dynamic reconfiguration of flow paths. Switching from serial injection to parallel distribution on the fly

provides a level of programmability previously unattainable in standard chromatography or flow chemistry setups.

Despite these strengths, the current iteration faces limitations common to meso-scale magnetic systems. The dynamic blocking threshold of ≈ 320 kPa indicates a constraint in the instantaneous force generation required to overcome high pneumatic loads during switching. We accept this trade-off for the system’s compact footprint. Future optimizations in coil density, core materials, and pulse shaping could extend this dynamic range. Additionally, while the current footprint suits benchtop automation and soft robotics perfectly, further miniaturization via MEMS fabrication techniques could integrate S-EPM logic directly into microfluidic chips. This would eliminate the need for off-chip interfaces entirely.

The S-EPM valve provides a robust, energy-efficient building block for the next generation of programmable matter. By eliminating the thermal and energetic penalties of continuous actuation, this technology paves the way for fully autonomous, untethered systems capable of complex chemical synthesis and sophisticated robotic motion.

3 Materials and Methods

S-EPM Fabrication

The Switchable-polarity ElectroPermanent Magnet (S-EPM) comprises a central low-coercivity Alnico 500 magnet surrounded by an excitation coil and flanked by two high-coercivity NdFeB magnets (N38SH) with opposing axial magnetizations. Soft-magnetic iron end caps enclose the assembly to complete the magnetic circuit and concentrate the external field at the pole interfaces.

We wound the excitation coil with 150 turns of 35 AWG copper wire. We achieved polarity switching using a single transient voltage pulse (48 V, 1 ms). This pulse reverses the remanent magnetization of the Alnico core and thereby toggles the external polarity. Each switching event consumed 0.6 J.

The SI Appendix provides detailed fabrication procedures and assembly steps.

Valve Assembly

The S-EPM valve integrates the bistable actuator within a compact pinch-valve architecture. We fabricated the housing using fused deposition modeling (FDM) 3D printing in PLA. We positioned two parallel silicone tubes (outer diameter 2 mm, inner diameter 1.5 mm) between the actuator end caps and internal raised support features to enable localized magnetic compression.

We arranged sixteen N40 permanent magnets (5 mm diameter \times 7 mm length) in four vertically aligned arrays surrounding the actuator. This generated a polarity-dependent magnetic force gradient. Magnets positioned along opposing vertical axes presented opposite poles toward the S-EPM, producing bidirectional actuation under polarity reversal.

The remanent polarity of the S-EPM (+1 and -1) defined the valve states, independent of the driving pulse once switching concluded.

Electrical Actuation

We generated transient excitation pulses using an H-bridge driver controlled by a microcontroller. Each switching event consisted of a single 1 ms voltage pulse (48 V). The pulse polarity determined the final remanent state of the S-EPM.

We applied no continuous holding current; magnetic remanence alone maintained the valve states. For multi-valve routing and decoder demonstrations, we addressed individual S-EPM units independently according to predefined state sequences.

The SI Appendix provides a detailed description of the electrical setup, including the driving circuitry and control architecture.

Pressure Characterization

We evaluated pressure blocking performance using regulated compressed air. We measured upstream (P_{in}) and downstream (P_{out}) pressures using amplified analog pressure transducers (Nidec P-7100 series). For low-pressure and compound measurements (-100 to 100 kPa), we used a P-7100-102R-M5 sensor (0.5 – 4.5 V analog output). For high-pressure characterization up to 1000 kPa, we employed a P-7100-103G-M5 gauge sensor (0.5 – 4.5 V analog output). We supplied both sensors at 5 V and calibrated them according to manufacturer specifications.

We conducted dynamic blocking tests up to 320 kPa. We performed static sealing tests at 300 kPa for 20 min and during stepwise pressure increases from 300 to 500 kPa. We extracted switching dynamics from time-resolved pressure traces.

Data Analysis

We recorded pressure signals digitally and converted them from voltage to pressure using the manufacturer-specified linear calibration. We extracted blocking thresholds and switching times directly from time-resolved pressure traces.

Programmable Fluidic Control and System-Level Demonstrations

Modular S-EPM valves were assembled into multiple configurations, including dual-tree, circular six-port, decoder, and mix-decoder architectures. Liquid (food dye) and air were used as working media under a constant driving pressure. Valve states ($+1$, -1) were applied according to predefined control sequences to achieve selective distribution, combinatorial mixing, and sequential addressing of output channels.

References

- [1] Ghazaleh Gharib, İsmail Bütün, Zülâl Munganlı, Gül Kozalak, İlayda Namlı, Seyedali Seyedmirzaei Sarraf, Vahid Ebrahimpour Ahmadi, Erçil Toyran, Andre J. van Wijnen, and Ali Koşar. Biomedical applications of microfluidic devices: A review. *Biosensors*, 12(11), 2022. ISSN 2079-6374. doi: 10.3390/bios12111023. URL <https://www.mdpi.com/2079-6374/12/11/1023>.
- [2] Yongxian Song, Yijiang Zhou, Kai Zhang, Zhaoxuan Fan, Fei Zhang, and Mingji Wei. Microfluidic programmable strategies for channels and flow. *Lab Chip*, 24:4483–4513, 2024. doi: 10.1039/D4LC00423J. URL <http://dx.doi.org/10.1039/D4LC00423J>.
- [3] Kevin McDonald and Tommaso Ranzani. Hardware methods for onboard control of fluidically actuated soft robots. *Frontiers in Robotics and AI*, Volume 8 - 2021, 2021. ISSN 2296-9144. doi: 10.3389/frobt.2021.720702. URL <https://www.frontiersin.org/journals/robotics-and-ai/articles/10.3389/frobt.2021.720702>.
- [4] Brooke Schuster, Michael Junkin, Sara Saheb Kashaf, Isabel Romero-Calvo, Kori Kirby, Jonathan Matthews, Christopher R. Weber, Andrey Rzhetsky, Kevin P. White, and Savaş Tay. Automated microfluidic platform for dynamic and combinatorial drug screening of tumor organoids. *Nature Communications*, 11(1):5271, October 2020. ISSN 2041-1723. doi: 10.1038/s41467-020-19058-4. URL <https://doi.org/10.1038/s41467-020-19058-4>.

- [5] Yi Jing Kerk, Aysha Jameel, Xin-Hui Xing, and Chong Zhang. Recent advances of integrated microfluidic suspension cell culture system. *Engineering Biology*, 5(4):103–119, December 2021. ISSN 2398-6182. doi: 10.1049/enb2.12015. URL <https://doi.org/10.1049/enb2.12015>. © 2021 The Authors. Engineering Biology published by John Wiley & Sons Ltd on behalf of The Institution of Engineering and Technology.
- [6] Yingjun Tian, Renbo Su, Xilong Wang, Nur Banu Altin, Guoxin Fang, and Charlie C. L. Wang. Openpneu: Compact platform for pneumatic actuation with multi-channels. In *2023 IEEE/ASME International Conference on Advanced Intelligent Mechatronics (AIM)*, pages 765–770, 2023. doi: 10.1109/AIM46323.2023.10196254.
- [7] Matheus S. Xavier, Charbel D. Tawk, Ali Zolfagharian, Joshua Pinski, David Howard, Taylor Young, Jiewen Lai, Simon M. Harrison, Yuen K. Yong, Mahdi Bodaghi, and Andrew J. Fleming. Soft pneumatic actuators: A review of design, fabrication, modeling, sensing, control and applications. *IEEE Access*, 10:59442–59485, 2022. doi: 10.1109/ACCESS.2022.3179589.
- [8] Lucas C. van Laake, Jelle de Vries, Sevda Malek Kani, and Johannes T.B. Overvelde. A fluidic relaxation oscillator for reprogrammable sequential actuation in soft robots. *Matter*, 5(9):2898–2917, 2022. ISSN 2590-2385. doi: <https://doi.org/10.1016/j.matt.2022.06.002>. URL <https://www.sciencedirect.com/science/article/pii/S2590238522002971>.
- [9] Hyung Gon Shin, Wan Kyun Chung, and Keehoon Kim. Soft and flexible robot skin actuator using multilayer 3d pneumatic network. *Nature Communications*, 16(1):5575, July 2025. ISSN 2041-1723. doi: 10.1038/s41467-025-60496-9. URL <https://doi.org/10.1038/s41467-025-60496-9>.
- [10] Toshihiro Nishimura, Kensuke Shimizu, Seita Nojiri, Kenjiro Tadakuma, Yosuke Suzuki, Tokuo Tsuji, and Tetsuyou Watanabe. Soft robotic hand with finger-bending/friction-reduction switching mechanism through 1-degree-of-freedom flow control. *IEEE Robotics and Automation Letters*, 7(2):5695–5702, 2022. doi: 10.1109/LRA.2022.3157964.
- [11] Shane Hoang, Konstantinos Karydis, Philip Brisk, and William H. Grover. A pneumatic random-access memory for controlling soft robots. *PLoS One*, 16(7):e0254524, July 2021. ISSN 1932-6203. doi: 10.1371/journal.pone.0254524. URL <https://doi.org/10.1371/journal.pone.0254524>. Research supported by U.S. Government (Non-P.H.S.).
- [12] Stephen T. Mahon, Jamie O. Roberts, Mohammed E. Sayed, Derek Ho-Tak Chun, Simona Aracri, Ross M. McKenzie, Markus P. Nimitz, and Adam A. Stokes. Capability by stacking: The current design heuristic for soft robots. *Biomimetics*, 3(3), 2018. ISSN 2313-7673. doi: 10.3390/biomimetics3030016. URL <https://www.mdpi.com/2313-7673/3/3/16>.
- [13] Muhsincan Sesen and Christopher J. Rowlands. Thermally-actuated microfluidic membrane valve for point-of-care applications. *Microsystems & Nanoengineering*, 7(1):48, June 2021. ISSN 2055-7434. doi: 10.1038/s41378-021-00260-3. URL <https://doi.org/10.1038/s41378-021-00260-3>.
- [14] Savita V. Kendre, Lauryn Whiteside, Tian Y. Fan, Jovanna A. Tracz, Gus T. Teran, Thomas C. Underwood, Mohammed E. Sayed, Haihui J. Jiang, Adam A. Stokes, Daniel J. Preston, George M. Whitesides, and Markus P. Nimitz. The soft compiler: A web-based tool for the design of modular pneumatic circuits for soft robots. *IEEE Robotics and Automation Letters*, 7(3):6060–6066, 2022. doi: 10.1109/LRA.2022.3159858.
- [15] Sihan Wang, Liang He, and Perla Maiolino. A modular approach to design multi-channel bistable valves for integrated pneumatically-driven soft robots via 3d-printing. *IEEE Robotics and Automation Letters*, 7(2):3412–3418, 2022. doi: 10.1109/LRA.2022.3147898.

- [16] Alan M. Gonzalez-Suarez, Alexander Long, XuHai Huang, and Alexander Revzin. A compact control system to enable automated operation of microfluidic bioanalytical assays. *Biosensors*, 12(12), 2022. ISSN 2079-6374. doi: 10.3390/bios12121160. URL <https://www.mdpi.com/2079-6374/12/12/1160>.
- [17] Kwang W Oh and Chong H Ahn. A review of microvalves. *Journal of Micromechanics and Microengineering*, 16(5):R13, mar 2006. doi: 10.1088/0960-1317/16/5/R01. URL <https://dx.doi.org/10.1088/0960-1317/16/5/R01>.
- [18] John V. Hinshaw. Valves for gas chromatography: Fundamentals. *LGC North America*, 29(3):246–251, March 2011. URL <https://www.chromatographyonline.com/view/valves-gas-chromatography-fundamentals-1>. Accessed: 2025-07-24.
- [19] Brian Keith Pederson and Brad Kevin Ahlgren. Fluid-directing multiport rotary valve, June 11 2013. US Patent 8,459,302.
- [20] Hua Gong, Adam T. Woolley, and Gregory P. Nordin. High density 3d printed microfluidic valves, pumps, and multiplexers. *Lab Chip*, 16:2450–2458, 2016. doi: 10.1039/C6LC00565A. URL <http://dx.doi.org/10.1039/C6LC00565A>.
- [21] Juliane Diehm, Verena Hackert, and Matthias Franzreb. Configurable 3d printed microfluidic multiport valves with axial compression. *Micromachines*, 12(10), 2021. ISSN 2072-666X. doi: 10.3390/mi12101247. URL <https://www.mdpi.com/2072-666X/12/10/1247>.
- [22] Nina Compera, Scott Atwell, Johannes Wirth, Bernhard Wolfrum, and Matthias Meier. Upscaling of pneumatic membrane valves for the integration of 3d cell cultures on chip. *Lab on a Chip*, 21(15):2986–2996, August 2021. ISSN 1473-0189. doi: 10.1039/d1lc00194a. URL <https://doi.org/10.1039/d1lc00194a>.
- [23] Daniel J. Preston, Haihui Joy Jiang, Vanessa Sanchez, Philipp Rothmund, Jeff Rawson, Markus P. Nemitz, Won-Kyu Lee, Zhigang Suo, Conor J. Walsh, and George M. Whitesides. A soft ring oscillator. *Science Robotics*, 4(31):eaaw5496, 2019. doi: 10.1126/scirobotics.aaw5496. URL <https://www.science.org/doi/abs/10.1126/scirobotics.aaw5496>.
- [24] S. Conrad, J. Teichmann, P. Auth, N. Knorr, K. Ulrich, D. Bellin, T. Speck, and F. J. Tauber. 3d-printed digital pneumatic logic for the control of soft robotic actuators. *Science Robotics*, 9(86):eadh4060, 2024. doi: 10.1126/scirobotics.adh4060. URL <https://www.science.org/doi/abs/10.1126/scirobotics.adh4060>.
- [25] Stephen T. Mahon, Anthony Buchoux, Mohammed E. Sayed, Lijun Teng, and Adam A. Stokes. Soft robots for extreme environments: Removing electronic control. In *2019 2nd IEEE International Conference on Soft Robotics (RoboSoft)*, pages 782–787, 2019. doi: 10.1109/ROBOSOFT.2019.8722755.
- [26] Colter J. Decker, Haihui Joy Jiang, Markus P. Nemitz, Samuel E. Root, Anoop Rajappan, Jonathan T. Alvarez, Jovanna Tracz, Lukas Wille, Daniel J. Preston, and George M. Whitesides. Programmable soft valves for digital and analog control. *Proceedings of the National Academy of Sciences*, 119(40):e2205922119, 2022. doi: 10.1073/pnas.2205922119. URL <https://www.pnas.org/doi/abs/10.1073/pnas.2205922119>.
- [27] Maks Gepner, Jonah Mack, and Adam A. Stokes. A standardized platform for translational advances in fluidic soft systems. *Device*, 3(8):100800, 2025. ISSN 2666-9986. doi: 10.1016/j.device.2025.100800. URL [https://www.cell.com/device/fulltext/S2666-9986\(25\)00113-9](https://www.cell.com/device/fulltext/S2666-9986(25)00113-9).

- [28] Ke Xu and Néstor O. Pérez-Arancibia. Electronics-free logic circuits for localized feedback control of multi-actuator soft robots. *IEEE Robotics and Automation Letters*, 5(3):3990–3997, 2020. doi: 10.1109/LRA.2020.2982866.
- [29] Jovanna A. Tracz, Lukas Wille, Dylan Pathiraja, Savita V. Kendre, Ron Pfisterer, Ethan Turett, Christoffer K. Abrahamsson, Samuel E. Root, Won-Kyu Lee, Daniel J. Preston, Haihui Joy Jiang, George M. Whitesides, and Markus P. Nimitz. Tube-balloon logic for the exploration of fluidic control elements. *IEEE Robotics and Automation Letters*, 7(2): 5483–5488, 2022. doi: 10.1109/LRA.2022.3156174.
- [30] Siyi Xu, Yufeng Chen, Nak seung P. Hyun, Kaitlyn P. Becker, and Robert J. Wood. A dynamic electrically driven soft valve for control of soft hydraulic actuators. *Proceedings of the National Academy of Sciences*, 118(34):e2103198118, 2021. doi: 10.1073/pnas.2103198118. URL <https://www.pnas.org/doi/abs/10.1073/pnas.2103198118>.
- [31] Metin Giousouf and Gabor Kovacs. Dielectric elastomer actuators used for pneumatic valve technology. *Smart Materials and Structures*, 22(10):104010, sep 2013. doi: 10.1088/0964-1726/22/10/104010. URL <https://dx.doi.org/10.1088/0964-1726/22/10/104010>.
- [32] Tiantian Huang, Denan Xu, Hang Zhang, Ou Bai, Aparna Aravelli, Xiaoxiao Zhou, and Bin Han. A lightweight flexible semi-cylindrical valve for seamless integration in soft robots based on the giant electrorheological fluid. *Sensors and Actuators A: Physical*, 347:113905, 2022. ISSN 0924-4247. doi: <https://doi.org/10.1016/j.sna.2022.113905>. URL <https://www.sciencedirect.com/science/article/pii/S0924424722005404>.
- [33] Alex Zatopa, Steph Walker, and Yigit Menguc. Fully soft 3d-printed electroactive fluidic valve for soft hydraulic robots. *Soft Robotics*, 5(3):258–271, 2018. doi: 10.1089/soro.2017.0019. URL <https://doi.org/10.1089/soro.2017.0019>. PMID: 29608429.
- [34] Sihan Wang, Liang He, Alessandro Albini, Peizhi Zhang, and Perla Maiolino. A magnetorheological elastomer-based proportional valve for soft pneumatic actuators. *Advanced Intelligent Systems*, 5(1):2200238, 2023. doi: <https://doi.org/10.1002/aisy.202200238>. URL <https://advanced.onlinelibrary.wiley.com/doi/abs/10.1002/aisy.202200238>.
- [35] Roman Balak and Yi Chen Mazumdar. Bistable valves for mr fluid-based soft robotic actuation systems. *IEEE Robotics and Automation Letters*, 6(4):8285–8292, 2021. doi: 10.1109/LRA.2021.3105687.
- [36] T Leps, P E Glick, D Ruffatto III, A Parness, M T Tolley, and C Hartzell. A low-power, jamming, magnetorheological valve using electropermanent magnets suitable for distributed control in soft robots. *Smart Materials and Structures*, 29(10):105025, sep 2020. doi: 10.1088/1361-665X/abadd4. URL <https://dx.doi.org/10.1088/1361-665X/abadd4>.
- [37] Kevin J. McDonald, Lorenzo Kinnicutt, Anna Maria Moran, and Tommaso Ranzani. Modulation of Magnetorheological Fluid Flow in Soft Robots Using Electropermanent Magnets. *IEEE Robotics and Automation Letters*, 7(2):3914–3921, April 2022. ISSN 2377-3766. doi: 10.1109/LRA.2022.3147873. URL <https://ieeexplore.ieee.org/abstract/document/9699046>.
- [38] Andrew D. Marchese, Cagdas D. Onal, and Daniela Rus. Soft robot actuators using energy-efficient valves controlled by electropermanent magnets. In *2011 IEEE/RSJ International Conference on Intelligent Robots and Systems*, pages 756–761, September 2011. doi: 10.1109/IROS.2011.6095064. URL <https://ieeexplore.ieee.org/abstract/document/6095064/authors>. ISSN: 2153-0866.

- [39] Anna Maria Moran, Vi T. Vo, Kevin J. McDonald, Pranav Sultania, Eva Langenbrunner, Jun Hong Vince Chong, Amartya Naik, Lorenzo Kinnicutt, Jingshuo Li, and Tommaso Ranzani. An electropermanent magnet valve for the onboard control of multi-degree of freedom pneumatic soft robots. *Communications Engineering*, 3(1):117, August 2024. ISSN 2731-3395. doi: 10.1038/s44172-024-00251-y. URL <https://doi.org/10.1038/s44172-024-00251-y>.
- [40] Azam Gholizadeh, Siamak Abbaslou, Pengfei Xie, Ara Knaian, and Mehdi Javanmard. Electronically actuated microfluidic valves with zero static-power consumption using electropermanent magnets. *Sensors and Actuators A: Physical*, 296:316–323, September 2019. ISSN 0924-4247. doi: 10.1016/j.sna.2019.06.037. URL <https://www.sciencedirect.com/science/article/pii/S0924424719301943>.
- [41] Alex E. Knaian. *Electropermanent magnetic connectors and actuators: devices and their application in programmable matter*. PhD thesis, Massachusetts Institute of Technology, 2010. URL <https://dspace.mit.edu/handle/1721.1/60151>. PhD Thesis, Department of Electrical Engineering and Computer Science at MIT.
- [42] Emily M. Werner. *A Programmable Droplet Microfluidic Liquid Handling Platform*. Phd dissertation, University of California, Irvine, 2021. URL <https://escholarship.org/uc/item/40b993xj>. ProQuest ID: Werner_uci_0030D_17039; Merritt ID: ark:/13030/m5jf13qv.
- [43] Kara Brower, Robert Puccinelli, Craig Markin, Tyler Shimko, Scott Longwell, Bianca Cruz, Rafael Gomez-Sjoberg, and Polly Fordyce. An open-source, programmable pneumatic setup for operation and automated control of single- and multi-layer microfluidic devices. *HardwareX*, 3, 10 2017. doi: 10.1016/j.ohx.2017.10.001.
- [44] Shaoxi Wang, Xiaofeng Zhang, Cong Ma, Sheng Yan, David Inglis, and Shilun Feng. A review of capillary pressure control valves in microfluidics. *Biosensors*, 11(10):405, 2021. doi: 10.3390/bios11100405. URL <https://doi.org/10.3390/bios11100405>.
- [45] Sebastian Steiner, Jakob Wolf, Stefan Glatzel, Anna Andreou, Jarosław M. Granda, Graham Keenan, Trevor Hinkley, Gerardo Aragon-Camarasa, Philip J. Kitson, Davide Angelone, and Leroy Cronin. Organic synthesis in a modular robotic system driven by a chemical programming language. *Science*, 363(6423):eaav2211, January 2019. doi: 10.1126/science.aav2211. URL <https://www.science.org/doi/10.1126/science.aav2211>. Publisher: American Association for the Advancement of Science.
- [46] Daniel Mark, Stefan Haeberle, Günter Roth, Felix von Stetten, and Roland Zengerle. Microfluidic lab-on-a-chip platforms: requirements, characteristics and applications. *Chem. Soc. Rev.*, 39:1153–1182, 2010. doi: 10.1039/B820557B. URL <http://dx.doi.org/10.1039/B820557B>.
- [47] Marco Pontin and Dana D. Damian. Multimodal soft valve enables physical responsiveness for preemptive resilience of soft robots. *Science Robotics*, 9(92):eadk9978, 2024. doi: 10.1126/scirobotics.adk9978. URL <https://www.science.org/doi/abs/10.1126/scirobotics.adk9978>.
- [48] Jungkyu Kim, Minsoung Kang, Erik C Jensen, and Richard A Mathies. Lifting the veil on microfluidic control systems. *Analytical chemistry*, 84(6):2950–2956, 2012.
- [49] Qinghai Zhang, Wei Yu, Jianghua Zhao, Chuizhou Meng, and Shijie Guo. A review of the applications and challenges of dielectric elastomer actuators in soft robotics. *Machines*, 13(2), 2025. ISSN 2075-1702. doi: 10.3390/machines13020101. URL <https://www.mdpi.com/2075-1702/13/2/101>.

- [50] Leonid Ionov. Hydrogel-based actuators: Possibilities and limitations. *Materials Today*, 17, 08 2014. doi: 10.1016/j.mattod.2014.07.002.
- [51] Michelle E. Peterson, Roy M. Daniel, Michael J. Danson, and Robert Eiseenthal. The dependence of enzyme activity on temperature: determination and validation of parameters. *Biochemical Journal*, 402(2):331–337, March 2007. ISSN 0264-6021. doi: 10.1042/BJ20061143.
- [52] Roy M. Daniel, Michael J. Danson, Robert Eiseenthal, Charles K. Lee, and Michelle E. Peterson. The effect of temperature on enzyme activity: new insights and their implications. *Extremophiles*, 12(1):51–59, January 2008. ISSN 1433-4909. doi: 10.1007/s00792-007-0089-7.